

Beyond the Lenormand phase diagram: Self-regulation mechanisms for controlling two-phase flows in porous media

Xiaokang Guo¹

¹Hebei University

December 22, 2022

Abstract

It is unclear why two-phase fluid flows in porous media develop a series of fluid displacement patterns. This study treats a two-phase flow system as an open thermodynamical system with a two-phase displacement process that follows the principle of the minimum operating power (MOPR). When different constraints are imposed on the system, the pore-scale interfacial dynamic response to this principle varies significantly, and a series of self-regulation mechanisms exist. These new findings not only explain the physical origins of the diverse fluid displacement patterns and interface reconstruction events but also provide new insights into the interface invasion protocol.

Hosted file

952606_0_art_file_10554714_rn812s.doc available at <https://authorea.com/users/568912/articles/614552-beyond-the-lenormand-phase-diagram-self-regulation-mechanisms-for-controlling-two-phase-flows-in-porous-media>

1 **Beyond the Lenormand phase diagram: Self-regulation**
2 **mechanisms for controlling two-phase flows in porous media**

3 Xiaokang Guo^{1,2,*}

4 ¹College of Civil Engineering and Architecture, Hebei University, Baoding,
5 071002, China

6 ²Technology Innovation Center for Testing and Evaluation in Civil Engineering of
7 Hebei Province, Hebei University, Baoding, 071002, China

8 *Corresponding author: guoxiaokang17@mails.ucas.edu.cn

9 **Abstract**

10 It is unclear why two-phase fluid flows in porous media develop a series of fluid
11 displacement patterns. This study treats a two-phase flow system as an open thermodynamical
12 system with a two-phase displacement process that follows the principle of the minimum
13 operating power (MOPR). When different constraints are imposed on the system, the
14 pore-scale interfacial dynamic response to this principle varies significantly, and a series of
15 self-regulation mechanisms exist. These new findings not only explain the physical origins of
16 the diverse fluid displacement patterns and interface reconstruction events but also provide
17 new insights into the interface invasion protocol.

18 **Plain Language Summary**

19 Why do immiscible two-phase fluid flows in porous media have a range of different fluid
20 distribution characteristics under different pore structures, fluid properties, and wettability
21 conditions? Does their occurrence follow a relatively uniform control principle? This study
22 demonstrated that the evolution direction of a two-phase flow system follows the principle of
23 the minimum operating power (MOPR). During the two-phase displacement process, the
24 system regulates itself through a series of self-regulation mechanisms to reduce the operating
25 power. A series of fluid displacement patterns can be regarded as the minimum operating power
26 states corresponding to a given displacement task under different system constraints, and the
27 formation of these patterns is inevitable, thereby preventing extra work for the system. These

28 findings provide new insights for the control of the interface invasion protocol that underlies
29 macroscopic flow properties.

30 **Keywords:** Displacement pattern; Minimum operating power principle;
31 Self-regulation mechanisms; Interface reconstruction events

32 **1. Introduction**

33 Immiscible two-phase fluid flows in porous media are important processes in natural and
34 engineered systems for carbon dioxide sequestration (CCS), enhanced oil recovery (EOR), and
35 nonaqueous phase liquid (NAPL) remediation, among other applications (Singh et al., 2019;
36 Holtzman and Segre, 2015; Zhao et al., 2016). The macroscopic flow properties are related to
37 interfacial instabilities at the pore scale, and understanding the flow behavior at the pore scale is
38 crucial for the optimal design of these processes. In the past few decades, to understand the
39 complexity of multiphase flows in porous media, scholars have conducted many numerical and
40 experimental studies to systematically explore the influencing mechanisms of various
41 characteristics, such as the pore structure, fluid properties and wettability, on two-phase flows
42 (Jiang et al., 2015; Zacharoudiou et al., 2020; Rokhforouz et al., 2019). At present, most studies
43 on two-phase displacement are conducted based on the Lenormand phase diagram and are
44 mainly from the perspective of force equilibrium, and the flow pattern dominating a given
45 displacement process can be determined by comparing the relative importance of gravity, the
46 viscous force, and the capillary force (Lenormand et al., 1988).

47 When gravity is negligible, the dynamics governing the fluid displacement pattern can be
48 characterized by two dimensionless numbers, namely, the capillary number ($Ca = \mu_i v_i / \sigma$)
49 and the viscosity ratio ($M = \mu_i / \mu_d$), where v is the characteristic velocity, σ is the
50 surface tension coefficient, μ is the viscosity coefficient, and the subscripts i and d
51 represent the invading phase and the displaced phase, respectively. When Ca is large and $M <$
52 1 , the viscous force dominates over the capillary force, and the fluid–fluid interface develops
53 dendritic structures along the flow direction, which is called viscous fingering (VF). In
54 contrast to $M < 1$, in the case of favorable viscosity ($M > 1$), the displacement front is viscous
55 stable, and the invading fluid scans the porous medium compactly, forming a stable

56 displacement (SD). For low Ca, the capillary force dominates over the viscous force, and an
57 intermittent fluid displacement process, called capillary fingering (CF), is observed. The
58 transition mode between these patterns is called a crossover zone (CZ).

59 In addition, wettability also plays an important role in the two-phase displacement
60 process. For example, Cieplak and Robbins (1990) proposed three modes of meniscus
61 motion (referred to as interface reconstruction events), namely, burst, contact, and overlap, and
62 they elucidated pore-scale displacement events at different wettabilities. Since then, in the
63 spirit of the Cieplak and Robbins model, the complex interactions between wettability and
64 pore geometry, along with the flow conditions, have been further investigated, thereby
65 extending the Cieplak-Robbins description of quasistatic fluid invasion and effectively
66 extending the classic Lenormand phase diagram (Basirat et al., 2017; Lin et al., 2021;
67 Jahanbakhsh et al., 2021; Jung et al., 2016; Hu et al., 2018). Clearly, the obtained Lenormand
68 phase diagram and related extended phase diagram based on the analysis of the force
69 equilibrium provide important insights into the dynamics of immiscible fluid displacement in
70 porous media. However, these studies did not fully elucidate the pore-scale flow physics behind
71 complex two-phase flow systems. For example, although transient dynamics during interface
72 reconstruction events have been extensively studied (Chen et al., 2019; Zacharoudiou et al.,
73 2016), it is generally believed that these events violate the hypothesis of slow displacement and
74 are a fast and irreversible process leading to energy dissipation. For example, Berg et al. (2013)
75 conducted energy conversion analysis based on 3D micro CT data and found that 64% of the
76 pressure volume work was dissipated through the Haines jump event. Hu et al. (2018) analyzed
77 the basic relationship between displacement mode conversion and energy conversion in rough
78 fracture two-phase flow. In the capillary state, approximately 51-58% of the surface energy is
79 dissipated by irreversible events. However, we believe that previous explorations of the
80 argument that the interface reconstruction event is an adverse energy mechanism have been
81 insufficiently rigorous. Among them, the physical origin of a series of fluid displacement
82 patterns or a series of interface reconstruction events is still unclear, and it is unknown if such
83 patterns and events follow a relatively unified control principle. Obviously, the previous

84 arguments based on the competition among the viscous force, capillary force and gravity
85 cannot provide a convincing physical explanation, and a new criterion is needed to study
86 immiscible displacement dynamics.

87 Based on the theory of nonequilibrium thermodynamics, in the linear nonequilibrium
88 region, an irreversible process in an open system always develops in the direction of
89 decreasing entropy production rate until the system reaches a nonequilibrium steady state that
90 satisfies the constraints. At this time, the entropy production rate is minimal under the
91 external constraints, which is called the principle of the minimum entropy production rate
92 (MEPR). The MEPR indicates the development and evolution direction of a dynamical
93 system, that is, no matter what its initial motion state is, if the system deviates from a stable
94 nonequilibrium state, its entropy production rate is not minimal, and the system must adjust
95 by reducing the entropy production rate until the entropy production rate reaches the
96 minimum and the system returns to a steady state. The MEPR has been demonstrated to be
97 very successful in explaining natural phenomena in both classical and modern physics (Xu et
98 al., 2016; Huang et al., 2004; Nanson et al., 2008; Jansen et al., 2004). According to
99 Nanson et al. (2008), rivers are natural “machines” that consume energy to perform work. In
100 river systems with surplus energy, the surplus energy can be consumed by adjusting the flow
101 wave characteristics and area. Xu et al. (2016) deduced the principle of the minimum energy
102 dissipation rate (MEDR) from the MEPR and verified the validity of the MEDR for alluvial
103 rivers using field data. When a river system is in a state of relative equilibrium, its energy
104 dissipation rate is minimal. Clearly, the MEPR, as a universal principle, is also applicable to
105 the field of two-phase flow in porous media.

106 For two-phase flow systems in porous media, although an immiscible fluid flow often
107 exhibits complex nonlinear behavior, unsteady turbulence is usually not involved; hence,
108 two-phase flow systems can be treated as linear nonequilibrium thermodynamic systems. A
109 two-phase displacement process follows not only the law of conservation of energy but also the
110 MEPR. However, in contrast to the fluvial dynamics systems described above, when two-phase
111 flows are involved, the presence of phase interfaces leads to a discontinuous fluid distribution

112 and a more complex energy balance field. Energy conversion usually occurs among the surface
113 energy, pressure–volume work, kinetic energy and dissipated energy, and the MEPR is not
114 simply equivalent to the MEDR. In this study, we found that the evolution direction of the
115 fluid displacement pattern follows a relatively unified control principle, that is, the principle
116 of the minimum operating power (MOPR). In addition, by clarifying the self-regulation
117 mechanism derived by the system that follows the MOPR principle, the physical origins of the
118 diversity of fluid displacement patterns can be explained.

119 **2. Flow patterns and analysis**

120 **2.1. Principle of the minimum entropy production rate**

121 In the context of the MEPR, in thermodynamics, an open system uses the least possible
122 energy to accomplish a given task, which includes constant single-phase flow and two-phase
123 displacement tasks. For a steady-state viscous single-phase flow, the system is in a stable
124 nonequilibrium state. In this paper, a principle equivalent to the MEPR is proposed, namely,
125 the MOPR. Specifically, in a control volume Ω with open boundaries, when a fluid flows in
126 at a constant flow rate Q (isothermal system), the operating power of the system can be
127 described as $P_o = \Delta p Q = \Phi$; that is, the power derived from the inlet and outlet pressure
128 difference $\Delta p = p_{int} - p_{out}$ through the system boundary is equal to the viscous dissipation
129 rate of the system Φ integrated over the entire porous domain (i.e., the entropy production
130 rate). The operating power P_o is clearly limited by the static constraints of the system
131 (including the pore structure, fluid properties, and boundary conditions, among others) and is
132 always minimal under the given constraints ($P_o = P_{min}$).

133 Although the evolution direction of a two-phase flow system still follows the MOPR,
134 the process of two-phase displacement includes both static and dynamic system constraints
135 (that is, the topology of the two-phase fluid). Even if the static constraints of the system remain
136 unchanged, the fluid topology is always undergoing a dynamic evolution process, causing the
137 system to deviate from a stable nonequilibrium state and the operating power P_o to no
138 longer be minimal, and the system develops in the direction of reduced operating power. Due

139 to the change in the fluid topology, the corresponding minimum operating power P_{\min} is no
 140 longer constant and may increase or decrease. Furthermore, compared to the simple energy
 141 conversion relationship of a steady-state single-phase flow system, the two-phase
 142 displacement process involves more energy terms, including pressure–volume work, surface
 143 energy, dissipated energy, and kinetic energy terms. The conversion form of the system
 144 operating power P_o changes significantly and is no longer equal to the viscous dissipation
 145 rate Φ . For an isothermal irreversible drainage process, the system operating power can be
 146 described as

$$147 \quad P_o = \Phi + \frac{dF_{surf}}{dt} + \frac{dE}{dt} \quad (1)$$

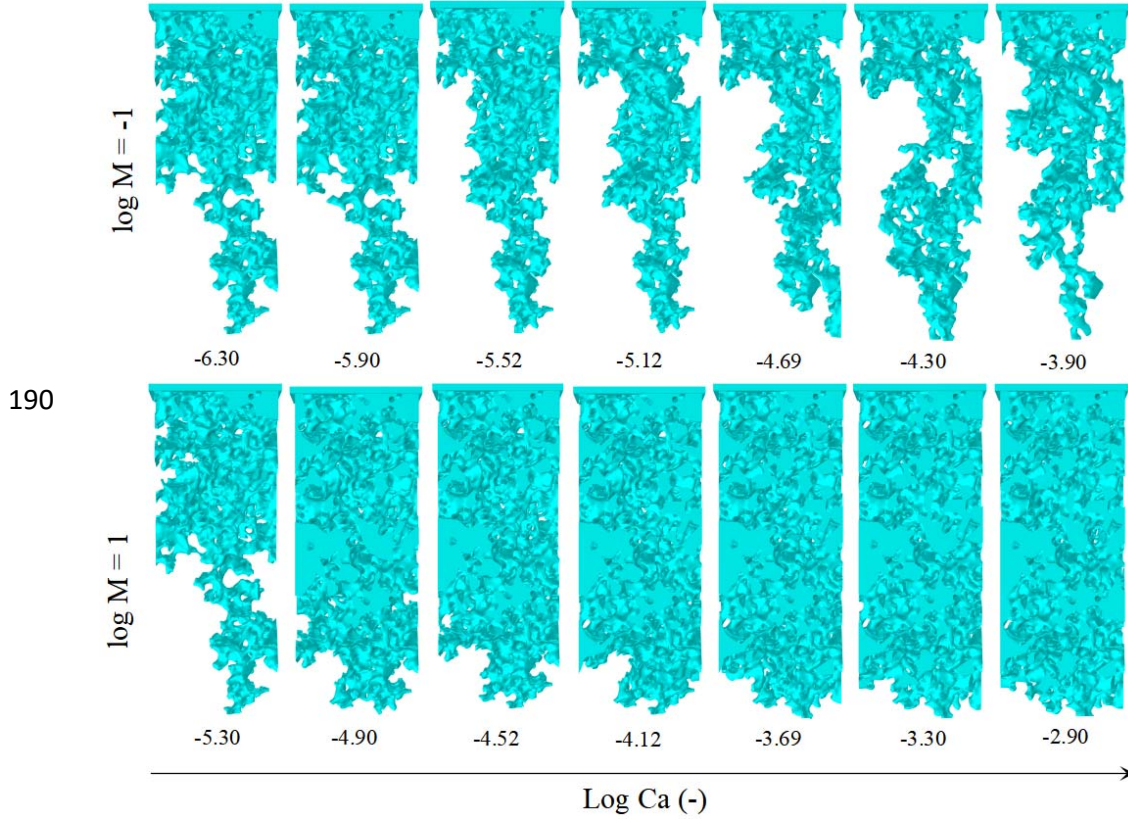
148 In Equation (1), the rate of energy introduction P_o into the system by the external
 149 pressure difference is equal to the sum of the viscous dissipation rate Φ , the rate of change in
 150 the surface energy dF_{surf}/dt , and the rate of change in the bulk kinetic energy dE/dt of the
 151 system. Among them, the viscous dissipation rate Φ of the system consists of the viscous
 152 dissipation rate of the invading phase Φ_i , the viscous dissipation rate of the displaced phase
 153 Φ_d , and the additional viscous dissipation rate due to inertial effects (inertial dissipation rate)
 154 Φ_n in the calculation domain. When inertial effects are not considered, Φ_n can be ignored.
 155 The rate of change in the surface energy dF_{surf}/dt consists of the rate of change in the
 156 solid-liquid surface energy $dF_{surf-s}/dt = |\cos\theta^{eq}| \sigma dA_{ns}/dt$ and the rate of change in the
 157 liquid-liquid surface energy $dF_{surf-f}/dt = \sigma dA_{int}/dt$, where A_{ns} is the nonwetting
 158 phase-solid interfacial area, and A_{int} is the fluid–fluid interfacial area.
 159 $dE/dt = \int_{\Omega} \frac{1}{2} \rho \mathbf{v} \cdot \mathbf{v} d\Omega / dt$ is the rate of change in the bulk kinetic energy, which consists of the
 160 rate of change in the kinetic energy of the invading phase dE_i/dt , the rate of change in the
 161 kinetic energy of the displaced phase dE_d/dt , and the rate of change in the kinetic energy of

162 the fluid phase discharged through system outlets dE_f/dt in the calculation domain.
163 Coupling effects exist among Φ , dF_{surf}/dt and dE/dt , and a change in one energy term
164 inevitably causes fluctuations in other energy contribution terms. As a result, different energy
165 terms contribute differently when the system approaches the minimum operating power state
166 ($P_o \rightarrow P_{min}$) under different constraints. Therefore, in contrast to the case of a steady-state
167 single-phase flow with no self-regulation mechanism, in the two-phase fluid displacement
168 process, the interface dynamics respond to the MOPR to derive a self-regulation mechanism.
169 The system regulates itself through this self-regulation mechanism to reduce the operating
170 power ($P_o \rightarrow P_{min}$). Under different constraints, the regulation mechanism for avoiding extra
171 work could be different and mainly depends on which energy contribution term is most
172 beneficial for controlling the system to approach the minimum operating power state.

173 **2.2. Self-regulation mechanisms**

174 To analyze a series of self-regulation mechanisms that govern interface dynamics and
175 fluid displacement patterns, a series of two-phase flow numerical simulations using a digital
176 core model are performed. A digital core model of the microscopic pore structure is
177 established by using computed tomography (CT), and the coupled Navier-Stokes and
178 Cahn-Hilliard equations are solved using the finite element method (with COMSOL
179 Multiphysics software) to capture the dynamic evolution of the flow front. For more details
180 on CT image processing and the phase field method (PFM), please refer to our previous work
181 (Guo et al., 2020). The main numerical results are presented in the form of a visual phase
182 diagram of the fluid distribution at breakthrough in a log Ca-log M plot, as shown in Fig. 1.
183 As Ca increases, the fluid displacement pattern changes from capillary fingering to viscous
184 fingering ($M < 1$) or stable displacement ($M > 1$). From the perspective of the Lenormand phase
185 diagram (force equilibrium), a series of fluid displacement patterns can be regarded as capillary
186 force-dominated and viscous force-dominated states. However, from the perspective of the
187 MOPR, a series of fluid displacement patterns can be regarded as displacement states at the

188 minimum operating power corresponding to the completion of the constant flow displacement
 189 task.



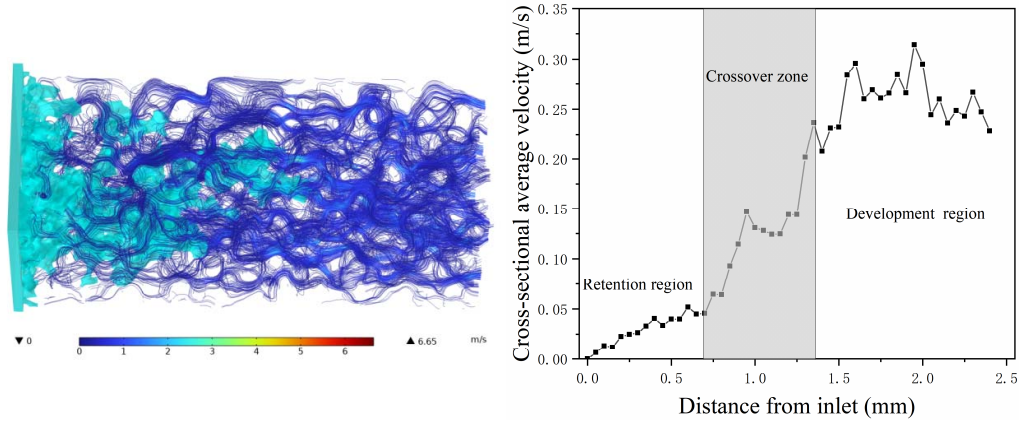
191 Figure 1. (a) Topological fluid distribution at the breakthrough time. The static contact angle
 192 θ^{eq} is set to 95° , which corresponds to weak drainage.

193 Specifically, for the viscous force-dominated state, the rate of energy introduction into
 194 the system by the external pressure difference P_o is approximately equal to the system
 195 viscous dissipation rate Φ , the rate of change in the surface energy dF_{surf}/dt and the rate
 196 of change in the kinetic energy dE/dt are negligible, and the conversion form of the system
 197 operating power P_o can be simplified to $P_o \approx \Phi$. Notably, in such a micron-scale pore
 198 system, despite the injection rate v_i being high, the rate of change in the kinetic energy
 199 dE/dt (integral term) can be ignored. According to Darcy's law, which is expressed as
 200 $\Delta p \approx -\mu LV/k$ (k is the medium permeability and L is the geometric length of the

201 medium), a fluid phase with a high viscosity flowing through a capillary channel at a constant
202 flow rate has a high viscosity dissipation. Therefore, for the VF state, under the MOPR
203 constraint, the system approaches the minimum operating power state mainly by regulating
204 the viscous dissipation rate of the displaced phase Φ_d . The system minimizes the area of the
205 displacement path of the invading phase to capture a large part of the displaced phase behind
206 the displacement front (the retained phase has a flow rate of 0 and $\Phi_d \rightarrow 0$). Although
207 shrinkage of the area of the displacement path of the invading phase can lead to an increase in
208 Φ_i ($A_i \downarrow$, $v_i \uparrow$, and $\Phi_i \uparrow$), the benefit of decreasing Φ_d caused by the increased retention
209 of the displaced phase is far greater than the loss caused by the increase in Φ_i . Moreover,
210 under the constraint of constant flow displacement, part of the displaced phase is always in
211 the migration state, and the system maximizes the area of the migration path of this part of the
212 displaced phase A_d to reduce the viscous dissipation rate of this part ($A_d \uparrow$, $v_d \downarrow$, and
213 $\Phi_d \downarrow$). Therefore, rapid formation of the main displacement path in the macroscopic
214 displacement direction is inevitable for the two-phase flow system to avoid extra work in the
215 VF state. Similarly, for the SD state, the system approaches the minimum operating power
216 state mainly by regulating the viscous dissipation rate of the invading phase Φ_i . That is, the
217 system maximizes the area of the displacement path of the invading phase to reduce the flow
218 velocity of the invading phase, thereby reducing the viscous dissipation rate of the invading
219 phase in the flow region ($A_i \uparrow$, $v_i \downarrow$, and $\Phi_i \downarrow$). Apparently, the loss of the increased Φ_d
220 due to the remigration of the retained displaced phase is much smaller than the benefit of the
221 decreased Φ_i due to the increase in the area of the displacement path of the invading phase.
222 Therefore, the invading phase compactly scans the porous medium, and the formation of
223 secondary flow paths beyond the primary displacement path is inevitable for the two-phase
224 flow system to avoid extra work in the SD state.

225 In this paper, the mechanism by which the development of the displacement interface in
 226 the VF or SD state always follows the displacement path with the minimum viscous dissipation
 227 rate is regarded as a self-regulation mechanism of the viscous dissipation rate ($\Phi_i \rightarrow \min$ or
 228 $\Phi_d \rightarrow \min$) and is demonstrated in Fig. 2(a,b). The fluid distributions and velocity field
 229 distributions in the VF and SD states and the local velocity distribution of the displaced phase
 230 along a cross-section of a porous medium sample are shown. For the VF state, the macroscopic
 231 response of the system to the self-regulation mechanism is reflected in the existence of a
 232 retention region and a development region of the displaced phase. In the retention region, the
 233 local velocity of the displaced phase remains relatively low, while in the development region,
 234 the local velocity distribution is uniform and well developed, fluctuating in the range of 0.207
 235 m/s–0.314 m/s. Of course, due to the dendritic structure of the invading fluid in the VF state,
 236 there is a clear CZ between the retention and development regions. In the SD state, there is no
 237 retention region, only a development region, and the CZ is narrower.

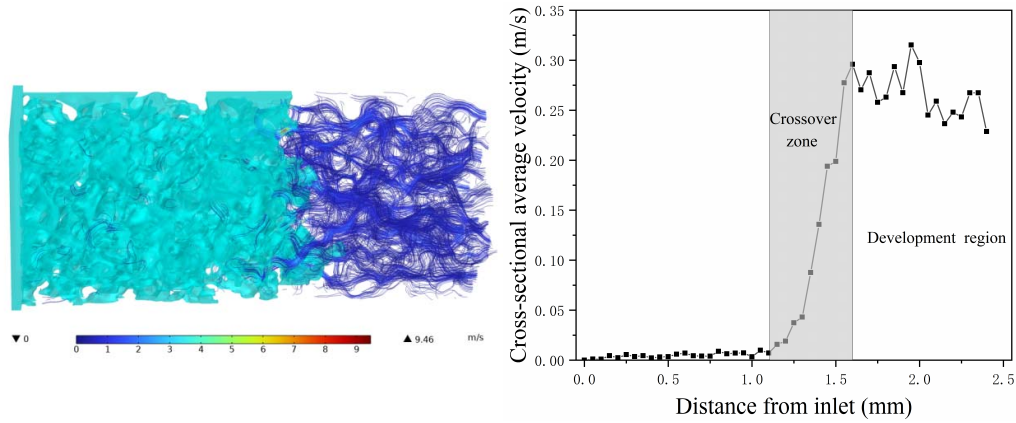
238



239

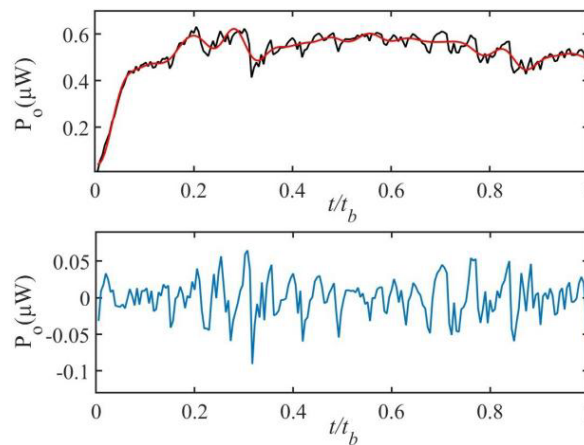
(a)

240



241

(b)



242

(c)

243

244 Figure 2. The fluid distribution of the invading phase and the velocity field distribution of the
 245 displaced phase at a certain time ($t/t_b = 0.649$) under different displacement patterns and the
 246 average velocity distribution of the displaced phase along a cross-section of a porous medium
 247 sample: (a) VF state ($\log Ca = -3.90$, $\log M = -1$) and (b) SD state ($\log Ca = -2.90$, $\log M = 1$).
 248 Low-speed and high-speed flow regions are shown in blue and red, respectively. (c) Evolution
 249 characteristics of the operating power P_o in the CF state ($\log Ca = -4.90$) with the normalized
 250 time t/t_b , where t is the penetration time and t_b is the breakthrough time ($t \leq t_b$). The bottom and
 251 top panels show the fluctuating component and the global trend of P_o , respectively.

252

253

254

The decrease in the capillary number Ca changes the relative importance of the viscous and capillary forces, resulting in a transition of the fluid displacement pattern from a viscous force-dominated state to a capillary force-dominated state. In the CF state, the reversible and

255 irreversible capillary force-dominated pore-scale displacement events alternate, which can be
256 demonstrated by the evolution characteristics of the operating power P_o , as shown in Fig. 2(c).
257 In this paper, the operating power signal is decomposed into global trend and fluctuation
258 components using wavelet decomposition (Primkulov et al., 2019). The global
259 low-frequency fluctuation trend of the operating power (red trend line in Fig. 2(c)) corresponds
260 to a reversible displacement event of meniscus invasion into the pore throat under a slow
261 displacement assumption, which is characterized by a uniform slow displacement at all
262 displacement interfaces. The rate of energy introduction P_o by the system pressure drop
263 during reversible displacement is approximately equal to the rate of surface energy change, the
264 viscous dissipation rate Φ and the rate of change in the kinetic energy dE/dt are negligible,
265 and the conversion form of the operating power P_o can be simplified to $P_o \approx dF_{surf}/dt$. That
266 is, P_o is regulated by dF_{surf}/dt , which is controlled by the geometrical structure of the
267 displacement path, which may increase or decrease, resulting in global low-frequency
268 fluctuations of P_o . In the context of the MORP, the system selects the most favorable
269 (minimum energy consumption) displacement path by comparing the rate of the surface
270 energy change of all potential moving menisci in different local pore throat regions.

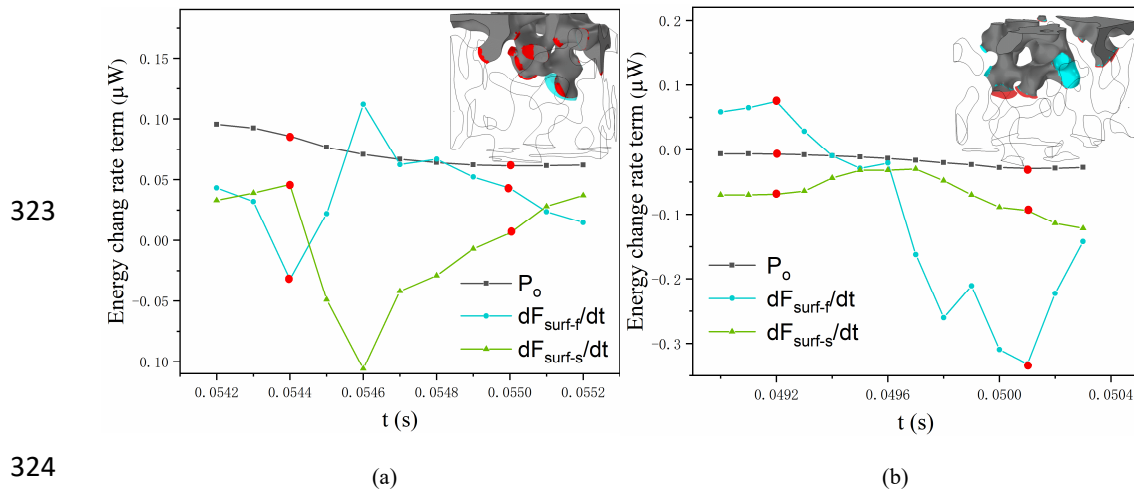
271 In this paper, the mechanism by which the development of the displacement interface in
272 the CF state always follows the displacement path of the minimum rate of surface energy
273 change is regarded as a self-regulation mechanism of the rate of the surface energy change
274 ($dF_{surf}/dt \rightarrow \min$). For a heterogeneous porous medium, deviation of the displacement path
275 from the macroscopic flow direction is clearly inevitable for the system to avoid excess energy
276 consumption, and the benefit from the reduction in dF_{surf}/dt due to the deviation of the
277 displacement path is much greater than the loss due to the possible increases in other energy
278 contribution terms. In addition, the high-frequency oscillations of the operating power P_o are
279 due to the rearrangement of the fluid phase (Haines jumps) as the meniscus migrates from the

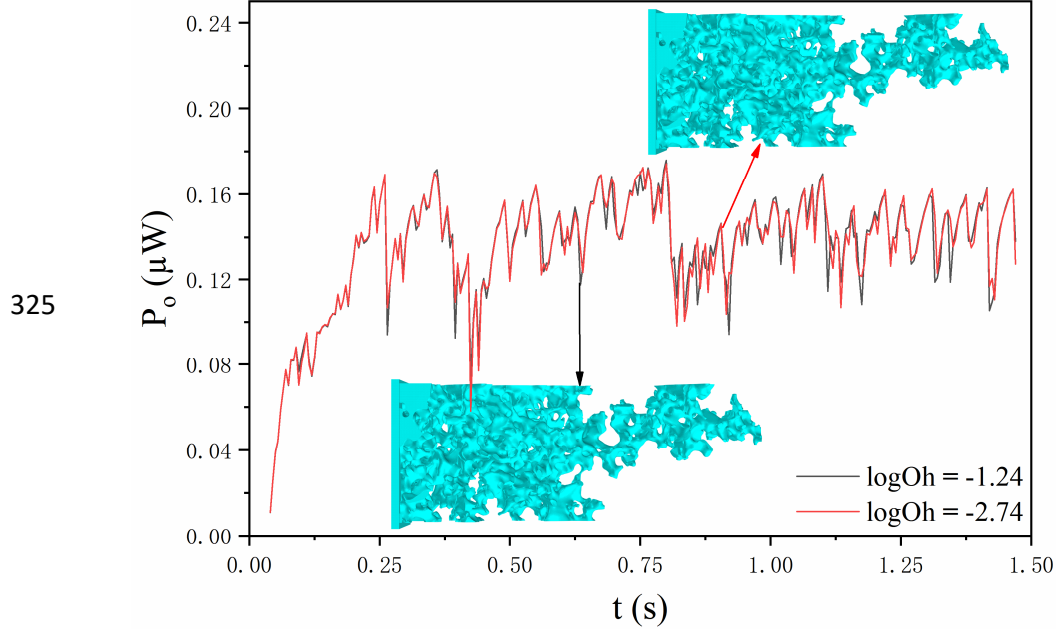
280 narrow pore throat to the wide pore body. Previous studies have suggested that during the
281 Haines jumps, the resulting local velocity is orders of magnitude larger than the injection
282 velocity, which greatly increases the energy dissipation. Clearly, the conversion form of the
283 operating power is also changed, and the viscous dissipation rate Φ can no longer be ignored.
284 The interface reconstruction events, such as Haines jumps, are discussed in Section 2.3.

285 **2.3. Physical origins of the interface reconstruction events**

286 These interface reconfiguration events are generally believed to cause partial driving energy to
287 be converted into viscous dissipated energy, which is a loss of driving energy and can be
288 regarded as an energy-adverse mechanism (Armstrong et al., 2015; Ferrari and Lunati, 2014;
289 O'Brien et al., 2020). However, from the perspective of the MOPR, an interface reconstruction
290 event is an irreversible change between the two most energetically favorable states, and it is an
291 energy favorable self-regulation mechanism derived from the system to avoid additional work
292 under specific constraints. Before an interface reconstruction event, the system is in the most
293 energetically favorable state (minimum surface energy state) under the current constraints
294 because the system follows the displacement path of the minimum rate of surface energy
295 change or the maximum rate of surface energy change. With the changes in the constraints
296 during the displacement process (the increase in the saturation S_i), a metastable fluid
297 configuration is generated. At this moment, any small change in the constraints, such as a slight
298 increase of S_i (reaching a specific constraint condition), may cause the system to no longer be
299 in a minimum surface energy state that satisfies the new constraints, and the fluid topology
300 can be redistributed (via Haines jump, contact or overlap events) to find the new energetically
301 most favorable state, as demonstrated in Fig. 3(a, b), which shows the fluid redistribution
302 associated with interfacial reconstruction events and the evolution characteristics of the
303 associated energy terms during interfacial reconstruction. As shown in Fig. 3(a), during the
304 Haines jump process, the conversion form of the operating power is
305 $P_o + \left| \frac{dF_{surf-s}^{rel}}{dt} \right| = \frac{dF_{surf-f}}{dt} + \Phi + \frac{dE}{dt}$. The sharp decline in the operating power P_o
306 indicates that P_o does not act ($P_o \rightarrow \min$), and the interfacial dynamics are mainly

307 controlled by $\left| \frac{dF_{surf-s}^{rel}}{dt} \right|$, which is provided by the reverse imbibition of the wetting phase in
 308 the adjacent pore throat. Therefore, during a Haines jump, to approach the new minimum
 309 surface energy state, the system maximally regulates the fluid topology to force the invading
 310 phase to move from a region with a high specific surface area to a region with a low specific
 311 surface area (as shown in the inset in Fig. 3(a), the invading phase retreats at the interface in the
 312 region with a high specific surface area). Likewise, as shown in Fig. 3(b), for a cooperative
 313 pore-filling event during imbibition, the conversion form of the operating power is
 314 $\left| \frac{dF_{surf-s}^{rel}}{dt} \right| + \left| \frac{dF_{surf-f}}{dt} \right| = |P_o| + \Phi + dE/dt$. The energy driving the interface
 315 reconstruction mainly originates from the surface energy, and the operating power P_o related
 316 to the external pressure difference is not involved. Therefore, during the approach to the new
 317 minimum surface energy state, the system maximally forces the invading phase to move from a
 318 region with a low specific surface area to a region with a high specific surface area (as shown in
 319 the inset in Fig. 3(b), the invading phase retreats at the interface in the region with a low
 320 specific surface area). Obviously, the operating power of the termination state of the interface
 321 reconfiguration event is far lower than the initial state, and the system reaches a new minimum
 322 operating power state.





327 Figure 3. The dynamic evolutions of P_o , dF_{surf-s}/dt and dF_{surf-s}/dt over time for
 328 different interfacial reconstruction events: (a) Haines jump event ($\theta = 115^\circ$), (b) cooperative
 329 pore-filling event ($\theta = 55^\circ$). The insets are snapshots of the corresponding fluid redistribution.
 330 The area occupied by the invading phase that remained unchanged after the interfacial
 331 reconstruction event is shown in gray, the advancing meniscus in the pore body and the
 332 receding menisci in the surrounding throats are shown in blue and red, respectively, and the red
 333 dots in the curve indicate the start and end of the interface reconstruction event. (c) Operating
 334 power P_o as a function of time for different Oh values in the CF state ($\log Ca = -6.3$, $\log M =$
 335 -1), where the Ohnesorge number $Oh = \sqrt{Ca/Re} = \mu_i / \sqrt{\rho_i \sigma d}$ reflects the relative importance of
 336 the inertial force to the viscous force and surface tension (in this paper, the fluid density ρ_i is
 337 controlled to change Oh while keeping Ca and M constant); d is the characteristic length,
 338 which is estimated as $d \approx \pi/S_v$ ($75 \mu\text{m}$); and S_v is the ratio of the pore-grain interface area to
 339 the total volume of the porous medium (Mostaghimi et al., 2020).

340 In addition, according to several recent studies, during interfacial reconfiguration events,
 341 inertial effects can significantly impact fluid invasion patterns in porous media (Zacharoudiou

342 et al., 2020; Ferrari et al., 2014). However, from the perspective of the MOPR, the minimum
343 surface energy state of the terminal state is only related to the geometric topology and the fluid
344 topology (minimum surface energy state of the initial state) but is not related to the transient
345 dynamics (inertial effects) during the interfacial reconstruction, as demonstrated in Fig. 3(c),
346 which shows the evolution of the operating power P_o with time for different Oh numbers.
347 The overall similar oscillation characteristics of the operating power P_o show that although
348 the Oh number changes by an order of magnitude, the transient dynamics associated with
349 inertial effects do not increase the operating power P_o , and their impact on the macroscopic
350 displacement patterns is very limited (as shown in the inset in Fig. 3(c)).

351 **3. Conclusions**

352 In this study, the minimum operating power principle, which is a fundamental principle
353 governing immiscible fluid flows, provides a convincing physical explanation for many
354 phenomena, including the physical origins of a series of fluid displacement patterns and
355 interfacial reconstruction events. When different constraints are imposed on a two-phase flow
356 system, the self-regulation mechanisms for the control system approaching the minimum
357 operating power state are significantly different. For example, when the self-regulation
358 mechanism of the viscous dissipation rate (for the displaced phase) dominates the displacement
359 process, the system inevitably forms a displaced phase retention region and development
360 region; when the self-regulation mechanism of the viscous dissipation rate (for an invading
361 phase) dominates the displacement process, the system inevitably increases the area of the
362 displacement path of the invading phase; and when the self-regulation mechanism of the rate of
363 surface energy change dominates the displacement process, for heterogeneous porous media,
364 the system inevitably introduces more curved displacement paths. In addition, a series of
365 interface reconstruction phenomena are no longer considered to be adverse energy events that
366 lead to rapid energy dissipation; rather, they are considered to be energy favorable
367 self-regulation mechanisms derived from the system to avoid additional work under specific
368 constraints.

369 **Data Availability Statement**

370 Relevant information of wavelet decomposition can be obtained from
371 <https://doi.org/10.5281/zenodo.7439463>.

372 **Acknowledgments**

373 This research was funded by the High-level Innovative Talents Program of Hebei
374 University (521100221059).

375 **References**

- 376 Singh K, Jung M, Brinkmann M, et al. Capillary-dominated fluid displacement in porous media[J].
377 Annual Review of Fluid Mechanics, 2019, 51: 429-449.
- 378 Holtzman R, Segre E. Wettability stabilizes fluid invasion into porous media via nonlocal,
379 cooperative pore filling[J]. Physical review letters, 2015, 115(16): 164501.
- 380 Zhao B, MacMinn C W, Juanes R. Wettability control on multiphase flow in patterned
381 microfluidics[J]. Proceedings of the National Academy of Sciences, 2016, 113(37):
382 10251-10256.
- 383 Jiang F, Tsuji T. Impact of interfacial tension on residual CO₂ clusters in porous sandstone[J].
384 Water Resources Research, 2015, 51(3): 1710-1722.
- 385 Zacharoudiou I, Boek E S, Crawshaw J. Pore-Scale Modeling of Drainage Displacement Patterns
386 in Association With Geological Sequestration of CO₂[J]. Water Resources Research, 2020,
387 56(11): e2019WR026332.
- 388 Rokhforouz M R, Amiri H A A. Effects of grain size and shape distribution on pore-scale
389 numerical simulation of two-phase flow in a heterogeneous porous medium[J]. Advances in
390 Water Resources, 2019, 124: 84-95.
- 391 Lenormand R, Touboul E, Zarcone C. Numerical models and experiments on immiscible
392 displacements in porous media[J]. Journal of fluid mechanics, 1988, 189: 165-187.
- 393 Cieplak M, Robbins M O. Influence of contact angle on quasistatic fluid invasion of porous
394 media[J]. Physical Review B, 41(16), 11508 (1990).
- 395 Basirat F, Yang Z, Niemi A. Pore-scale modeling of wettability effects on CO₂-brine displacement
396 during geological storage[J]. Advances in water resources, 109, 181-195 (2017).

397 Lin W, Xiong S, Liu Y, et al. Spontaneous imbibition in tight porous media with different
398 wettability: Pore-scale simulation[J]. *Physics of Fluids*, 32(3), 032013 (2021).

399 Jahanbakhsh A, Shahrokhi O, et al. Understanding the role of wettability distribution on
400 pore-filling and displacement patterns in a homogeneous structure via quasi 3D pore-scale
401 modelling[J]. *Scientific Reports*, 11, 17847 (2021).

402 Jung M, Brinkmann M, Seemann R, et al. Wettability controls slow immiscible displacement
403 through local interfacial instabilities[J]. *Physical Review Fluids*, 1(7), 074202 (2016).

404 Hu R, Wan J, Yang Z, et al. Wettability and flow rate impacts on immiscible displacement: A
405 theoretical model[J]. *Geophysical Research Letters*, 2018, 45(7): 3077-3086.

406 Chen Y, Valocchi A J, Kang Q, et al. Inertial effects during the process of supercritical CO₂
407 displacing brine in a sandstone: Lattice Boltzmann simulations based on the
408 continuum-surface-force and geometrical wetting models[J]. *Water Resources Research*, 2019,
409 55(12): 11144-11165.

410 Zacharoudiou I, Boek E S. Capillary filling and Haines jump dynamics using free energy Lattice
411 Boltzmann simulations[J]. *Advances in water resources*, 2016, 92: 43-56.

412 Berg S, Ott H, Klapp S A, et al. Real-time 3D imaging of Haines jumps in porous media flow[J].
413 *Proceedings of the National Academy of Sciences*, 2013, 110(10): 3755-3759.

414 Hu R, Wu D S, Yang Z, et al. Energy conversion reveals regime transition of imbibition in a rough
415 fracture[J]. *Geophysical Research Letters*, 2018, 45(17): 8993-9002.

416 Xu G, Zhao L, Yang C T. Derivation and verification of minimum energy dissipation rate principle
417 of fluid based on minimum entropy production rate principle[J]. *International Journal of*
418 *Sediment Research*, 2016, 31(1): 16-24.

419 Huang H Q, Chang H H, Nanson G C. Minimum energy as the general form of critical flow and
420 maximum flow efficiency and for explaining variations in river channel pattern[J]. *Water*
421 *Resources Research*, 2004, 40(4).

422 Nanson G C, Huang H Q. Least action principle, equilibrium states, iterative adjustment and the
423 stability of alluvial channels[J]. *Earth Surface Processes and Landforms: The Journal of the*
424 *British Geomorphological Research Group*, 2008, 33(6): 923-942.

425 Jansen J D, Nanson G C. Anabranching and maximum flow efficiency in Magela Creek, northern
426 Australia[J]. Water Resources Research, 2004, 40(4).

427 Guo X, Liu R, Wang J, et al. Pore-scale modeling of wettability effects on infiltration behavior in
428 liquid composite molding[J]. Physics of Fluids, 2020, 32(9): 093311.

429 COMSOL Multiphysics® v. 5.4. COMSOL AB. Retrieved from www.comsol.com

430 Primkulov B K, Pahlavan A A, Fu X, et al. Signatures of fluid–fluid displacement in porous
431 media: wettability, patterns and pressures[J]. Journal of Fluid Mechanics, 2019, 875.

432 Armstrong R T, Evseev N, Koroteev D, et al. Modeling the velocity field during Haines jumps in
433 porous media[J]. Advances in Water Resources, 2015, 77: 57-68.

434 Ferrari A, Lunati I. Inertial effects during irreversible meniscus reconfiguration in angular pores[J].
435 Advances in water resources, 2014, 74: 1-13.

436 O'Brien A, Afkhami S, Bussmann M. Pore-scale direct numerical simulation of Haines jumps in a
437 porous media model[J]. The European Physical Journal Special Topics, 2020, 229(10):
438 1785-1798.

439 Mostaghimi P, Bijeljic B, Blunt M J. Simulation of flow and dispersion on pore-space images[J].
440 SPE Journal, 2012, 17(04): 1131-1141.

441